crystals

MDPI

Article

Influence of the Crystal Surface on the Austenitic and Martensitic Phase Transition in Pure Iron

Jerome Meiser and Herbert M. Urbassek *

Physics Department and Research Center OPTIMAS, University Kaiserslautern, Erwin-Schrödinger-Straße, D-67663 Kaiserslautern, Germany

* Correspondence: urbassek@rhrk.uni-kl.de; Tel.: +49-631-205-3022

Received: 22 November 2018; Accepted: 12 December 2018; Published: 14 December 2018

Abstract: Using classical molecular dynamics simulations, we studied the influence that free surfaces exert on the austenitic and martensitic phase transition in iron. For several single-indexed surfaces—such as $(100)_{bcc}$ and $(110)_{bcc}$ as well as $(100)_{fcc}$ and $(110)_{fcc}$ surfaces—appropriate pathways exist that allow for the transformation of the surface structure. These are the Bain, Mao, Pitsch, and Kurdjumov–Sachs pathways, respectively. Tilted surfaces follow the pathway of the neighboring single-indexed plane. The austenitic transformation temperature follows the dependence of the specific surface energy of the native bcc phase; here, the new phase nucleates at the surface. In contrast, the martensitic transformation temperature steadily decreases when tilting the surface from the $(100)_{fcc}$ to the $(110)_{fcc}$ orientation. This dependence is caused by the strong out-of-plane deformation that $(110)_{fcc}$ facets experience under the transformation; here, the new phase also nucleates in the bulk rather than at the surface.

Keywords: solid–solid phase transition; molecular dynamics simulation; iron; surface

1. Introduction

Solid–solid phase transformations, such as the well-known α–γ transition occurring in pure iron and in steels, play an important role in the behavior of these materials and in technological applications [1,2]. In the recent past, atomistic simulations have been used to obtain insight into the dynamics of this transformation [3,4]. While many aspects have been investigated, the influence of crystal defects on the transformation path is still under discussion. Thus, it has been found that grain boundaries [5,6], other planar defects such as stacking faults [7] and dislocations [8–10] may act as nucleation sites for the transformation. In addition, phase boundaries [11–14] and heterogeneous interfaces, such as with carbide phases [15], affect the transformation behavior; in these cases, of course, the crystal orientation at the interface is decisive.

Surfaces provide another source of planar defect that may influence the transformation. Despite the inevitable presence of surfaces, their role in the transformation process does not appear to have been thoroughly investigated up to now [16]. Surfaces provide free volume, which facilitates the cooperative motion necessary for the transformation. In addition, the potential energy stored in surfaces with high specific surface energy may be used to trigger the transformation [17]. In nanowires, it has even been found that the surface stress may induce a phase transformation that does not exist in the bulk, such as from fcc-Au phase to bct-Au phase [18]. On the other hand, the pathway followed during the transformation may not agree with the surface orientation—in the sense that the surface plane is not conserved during the transformation—and thus delay or even impede the transformation.

We used molecular dynamics simulation to investigate the influence that the surface exerts on the α-γ transition in pure iron; both the $\alpha \rightarrow \gamma$ transition—denoted for convenience as the "austenitic" transformation—and the $\gamma \rightarrow \alpha$ transition—the "martensitic" transformation—were considered.

We concentrated on (100) and (110) surfaces as well as [001] tilt surfaces that interpolate between these two. Thus, our study allowed identifying the influence of the specific surface energy and the surface orientation on the transformation pathway and the transformation temperature.

2. Simulation Method

We studied (100) and (110) surfaces of face-centered-cubic (fcc) and body-centered-cubic (bcc) Fe, as well as the higher-indexed (h k 0) planes interpolating between (100) plane and (110) plane. They can be described by the tilt angle towards (100) plane, ϕ, given by

$$\sin\phi = \frac{k}{\sqrt{h^2+k^2}}, \tag{1}$$

which denotes the rotation angle around the [001] axis, as indicated in Figure 1. This figure also introduces our coordinate system; the z axis points normal to the free surface, while the y axis is the [001] direction. Table 1 lists the surfaces studied in this investigation.

Our samples were thin films containing two free surfaces in z direction; in x and y direction, we employed periodic boundary conditions to mimic laterally infinitely extended surfaces. Note that tilted surfaces exhibit a periodicity with a length of

$$d = a\sqrt{h^2+k^2}, \tag{2}$$

where a denotes the lattice constant. Correspondingly, the system size must be chosen such that an integer number of these period fits into the lengths of the simulation volume in x and z direction cf. Figure 1. The length in y direction was chosen as an integer multiple of a. The simulation systems contained roughly 22,000 atoms. We created bcc crystallites to study the austenitic transformation; these have extensions of approximately 64 Å × 64 Å × 64 Å in x, y, z direction, respectively; the exact numbers depended on the periodicity length d, and hence on the surface studied. Analogously, for the study of the martensitic transformation, we created fcc crystallites with extensions of 80 Å × 80 Å × 40 Å. The effect of the system size on the transformation behavior is presented in the Appendix.

The samples were relaxed using the method of energy minimization by conjugate gradients [19] at 0 K. Then, we equilibrated the systems for 10 ps at the starting temperature. The starting temperature was 10 K for the austenitic transition, and 400 K for the martensitic transition. The transformations were induced by heating or cooling the system at a prescribed rate, i.e., 1 K/ps for the austenitic transformation and 0.33 K/ps for the martensitic transformation. During heating/cooling, the temperature was controlled by a Nose–Hoover thermostat [20,21], and the Cartesian components of the pressure were kept constant at zero by a barostat. This means that we accomplished strain accommodation not only in the direction normal to the surface, but also within the surface plane. The phase transformation temperature, T_c, was determined from the change of the volume size with temperature; a sudden jump of the system volume indicates the transformation.

Iron atoms interact via the Meyer–Entel interaction potential [22], which implements the phase transition between the α and γ phase [23]. Note that the equilibrium transition temperature T_c of this potential is 550 ± 50 K, as determined by both free-energy calculations [23,24] and dynamic molecular dynamics simulations [25,26]. This temperature is smaller than in experiment (1184 K); this feature of the Meyer–Entel potential is well-known and implies that the results presented here need to be scaled appropriately to apply to realistic systems.

All calculations were performed with the open-source LAMMPS code [27]. The local lattice structure was determined by the common-neighbor analysis (CNA) [28,29]. The free software tool OVITO [30] was used for visualization of the local structure of the atoms.

The surface energy, E_{surf}, was calculated from the energy difference of a thin film (containing two surfaces, each of area A) and a bulk material containing the same number of atoms, N:

$$E_{\mathrm{surf}} = \frac{E_{\mathrm{tot}} - N \cdot E_{\mathrm{coh}}}{2A}. \quad (3)$$

where E_{tot} is the potential energy of the thin-film system and E_{coh} is the cohesive energy. The surface energies increased for bcc-Fe in the order of (110), (100), and (111); and for fcc-Fe in the order of (111), (100), and (110). This order is the same as that found in previous studies [31,32]. We note, however, that the magnitude of the surface energies obtained for the Meyer–Entel potential was somewhat smaller than in experiment [32]. For the Meyer–Entel potential, the cohesive energy was 4.2784 (4.2407) eV for the bcc (fcc) structure; the lattice constant was 2.8655 (3.6862) Å.

Table 1. Surfaces studied in the bcc and fcc samples. ϕ denotes the tilt angle towards the (100) plane (Equation (1)).

(*h k* 0)	ϕ (degree)
(1 0 0)	0
(11 1 0)	5.195
(7 1 0)	8.13
(3 1 0)	18.435
(2 1 0)	26.57
(3 2 0)	33.69
(1 1 0)	45

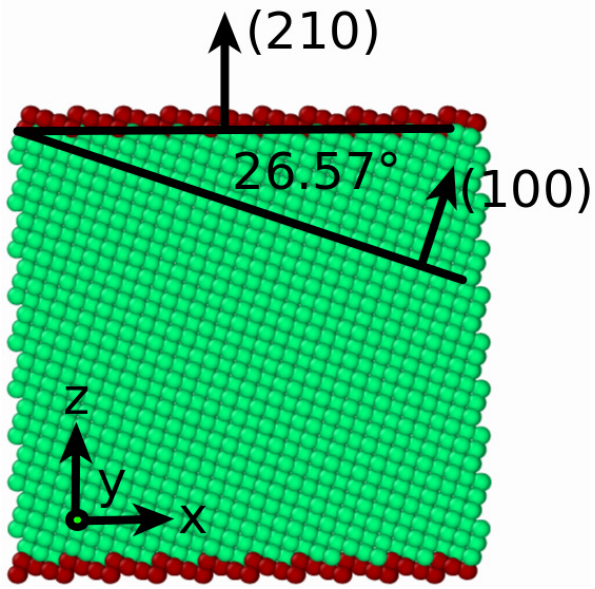

Figure 1. Side view of a bcc sample with a (210) surface. The tilt angle ϕ towards the (100) plane (Equation (1)) is indicated. Colors denote the local crystal structure. Green, bcc; dark blue, fcc; light blue, hcp; red, unknown.

3. Austenitic Transformation

As a reference, we first note that we also simulated the transformation of bulk iron in the absence of any surface; this was done by using periodic boundary conditions in all Cartesian directions. For a system with 22528 atoms in a cubic box of 64.83 Å edge length, we found a T_c of 1458 K. In the following, we report on how the presence of a surface may lower the phase transition temperature.

3.1. (100) Surface

We first studied the austenitic transformation of a $(100)_{\mathrm{bcc}}$ surface. Figure 2 demonstrates that the material completely transforms into the fcc structure, without any defects formed. An inspection of the atomistics of the surface shows that that $(100)_{\mathrm{bcc}}$ surface was transformed to the $(100)_{\mathrm{fcc}}$ surface. In addition, the $(010)_{\mathrm{bcc}}$ direction and the $(001)_{\mathrm{bcc}}$ direction were transformed into the $(011)_{\mathrm{fcc}}$ direction and the $(01\bar{1})_{\mathrm{fcc}}$ direction, respectively. This is the classical Bain orientation relationship [33]:

$$\begin{aligned} &(100)_{\mathrm{bcc}} \parallel (100)_{\mathrm{fcc}}, \\ &[010]_{\mathrm{bcc}} \parallel [011]_{\mathrm{fcc}}, \quad [001]_{\mathrm{bcc}} \parallel [01\bar{1}]_{\mathrm{fcc}}\,. \end{aligned} \tag{4}$$

During the transformation, the surface area shrunk by 18 %. In addition, the (specific) surface energy also decreased from a value of 1.73 J/m^2 for the $(100)_{\mathrm{bcc}}$ surface to a value of 1.57 J/m^2 for the $(100)_{\mathrm{fcc}}$ surface. In total, the gain in surface energy assisted the transformation. The transition temperature was $T_c = 615$ K; compared to the values cited below, this is a rather small value.

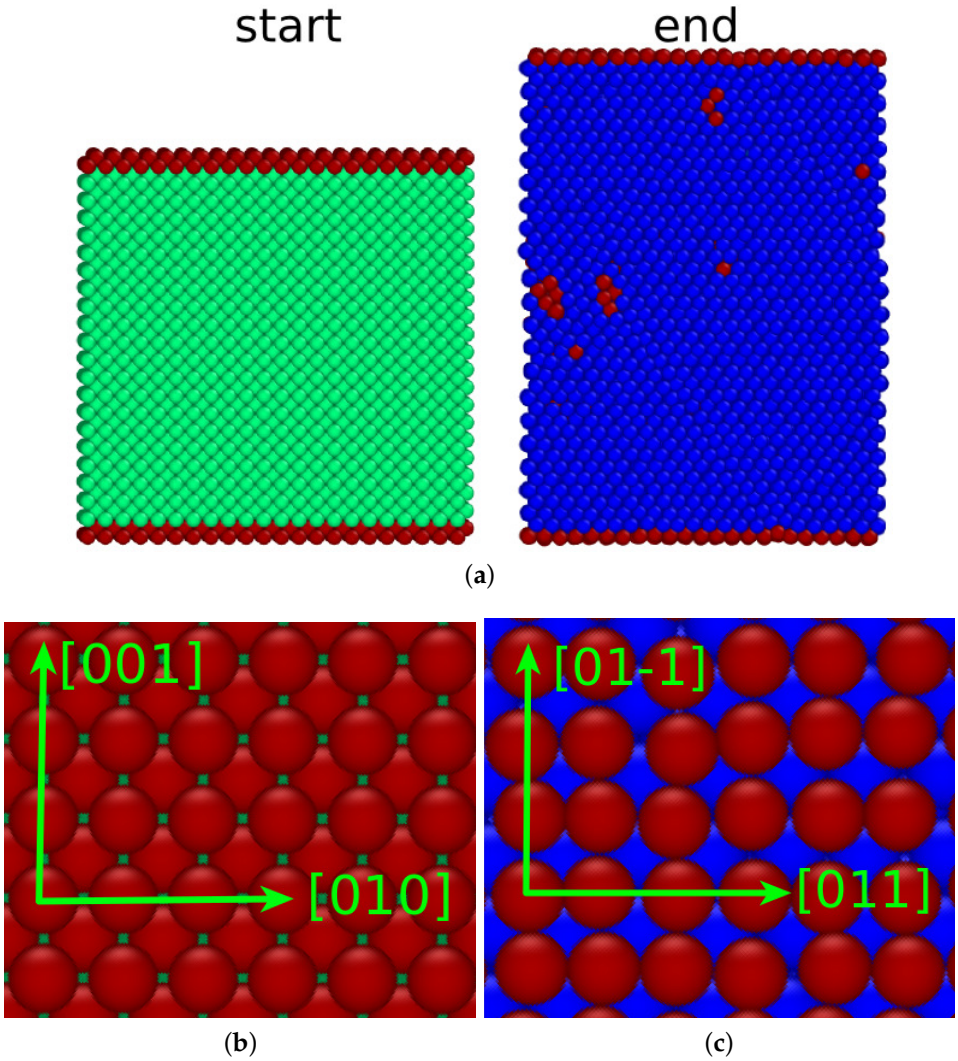

Figure 2. Austenitic transformation of a thin-film bcc Fe slab with a $(001)_{\mathrm{bcc}}$ surface: (**a**) side view of the film before and after the transformation; (**b**) top views of the film before the transformation; and (**c**) top views of the film after the transformation. The green arrows highlight the conserved directions. Colors denote the local lattice structure as in Figure 1.

3.2. (110) surface

The transformation of a bcc crystal with a (110) surface proceeded very differently. While the bcc lattice transformed completely to a close-packed structure, it resulted in hcp rather than fcc phase. Note that the energy difference between the two close-packed phases—hcp and fcc— in the Meyer–Entel potential is tiny, i.e., 2.9 meV/atom, while the bcc phase has a 40 meV/atom smaller energy [25,34]. In simulation studies of the austenitic transformation in Fe, typically both close-packed phases, fcc and hcp, are created [16,35,36].

Figure 3a shows the sample before and after the phase transition. The changes in surface area (-7%) and crystal thickness are considerably smaller than for the (100) surface. We see that the $(1\bar{1}0)_{\mathrm{bcc}}$ plane perpendicular to the surface was conserved over the phase transition and transforms into the $(0001)_{\mathrm{hcp}}$ plane. Stacking fault planes run perpendicular to the surface. Their creation leads to a considerable roughening of the surface.

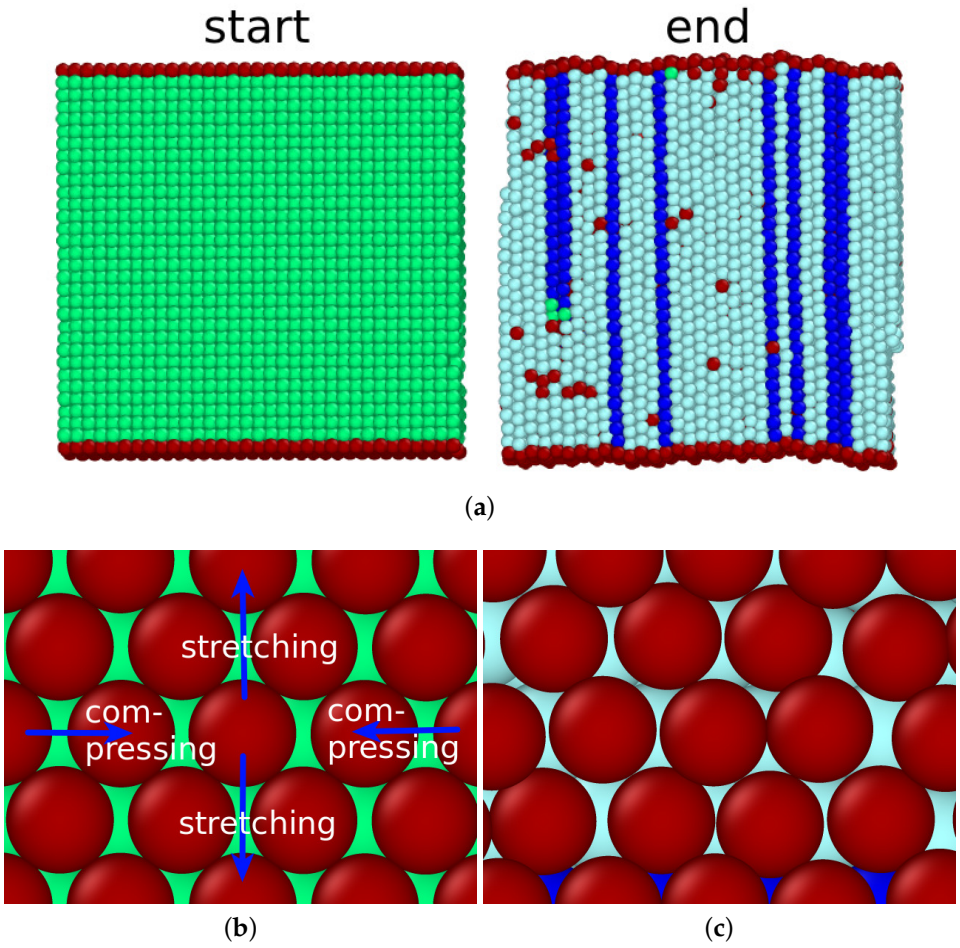

Figure 3. Austenitic transformation of a thin-film bcc Fe slab with a (110) surface: (**a**) side view of the film before and after the transformation; (**b**) top views of the film before the transformation; and (**c**) top views of the film after the transformation. The blue arrows highlight the directions, in which the crystal is compressed or stretched during the transformation. Colors denote the local lattice structure as in Figure 1.

An atomistic view of the conserved planes (Figure 3b,c) shows how the transition occurs in this plane. The $[110]_{\mathrm{bcc}}$ direction transforms into the $[0\bar{1}10]_{\mathrm{hcp}}$ direction by an expansion. while the

$[001]_{bcc}$-direction transforms into the $[\bar{2}110]_{hcp}$ direction by a compression. This transition process was described by Mao et al. [37] and Wang and Ingalls [38]:

$$(1\bar{1}0)_{bcc} \parallel (0001)_{hcp},$$
$$[001]_{bcc} \parallel [\bar{2}110]_{hcp}, \quad [110]_{bcc} \parallel [0\bar{1}10]_{hcp}. \tag{5}$$

It is the bcc–hcp analog to the Nishiyama–Wassermann [39,40] pathway for the bcc–fcc phase transition. We may assume that, if the Meyer–Entel potential preferred the fcc structure, we would probably see the Nishiyama–Wassermann pathway for this surface.

The specific surface energy of the original $(110)_{bcc}$ surface is 1.35 J/m^2. After the transformation, $(0001)_{hcp}$ has an energy of 1.33 J/m^2. Both values are small, since the surfaces are close-packed. The small energy difference between the surface structures is compatible with a high transformation temperature, $T_c = 987$ K.

3.3. (111) Surface

We could not observe the austenitic transformation of thin slabs with $(111)_{bcc}$ surfaces, even when heating the specimen up to 2000 K. Note that the bulk specimen transformed already at 1485 K; hence, it appears that the (111) surface actually impedes a transformation that would have occurred in the absence of any surface. Even homogeneous nuclei—that started the transformation in the bulk specimen—would not lead to the transformation in thin slabs bounded by the $(111)_{bcc}$ surface. When analyzing the bulk transformation behavior in detail, we observed that it was governed by the Bain path, similar to the thin film with a $(100)_{bcc}$ surface. This path is, however, not available for the $(111)_{bcc}$ surface, since the $(111)_{bcc}$ surface plane was not conserved in this transformation path; actually, it was not conserved in any of the transformation pathways observed in our study. Hence, the nucleation of the close-packed phase at this surface was impeded. If the transformation started homogeneously in the bulk following the Bain path, the $(111)_{bcc}$ surfaces were subjected to strong deformations, similar to the transformation of the $(110)_{fcc}$ surface presented in Section 4.2. Even the high specific surface energy of 1.76 J/m^2 did not help to induce the phase transition. We conclude that this surface works rather as an obstacle to the phase transition.

3.4. Tilted Surfaces

3.4.1. Specific Surface Energy and Phase Transition Temperature

The surfaces used in this study are assembled in Table 1. We display in Figure 4a the variation of the specific surface energy on the tilt angle. The $(100)_{bcc}$ surface, $\phi = 0°$, has a rather high specific surface energy of 1.73 J/m^2, while the $(110)_{bcc}$, $\phi = 45°$, is close-packed and has a low specific surface energy of 1.35 J/m^2. Slight misorientations from the $(100)_{bcc}$ surface lead to faceting; the surface develops steps, so that the specific surface energy increases somewhat. Beyond a maximum at around 10°–15°, the energy decreases with the packing density of the surface.

All these tilted surfaces show an austenitic transformation upon heating. Figure 4b displays the transformation temperatures T_c. Note that T_c and E_{surf} are anticorrelated; the surfaces with the highest values of E_{surf} transform most easily, i.e., at the lowest temperatures. In addition, note that all transformation temperatures are lower than for the bulk sample, $T_c = 1458$ K; the existence of a surface lowers the phase transition temperature for all surfaces investigated here.

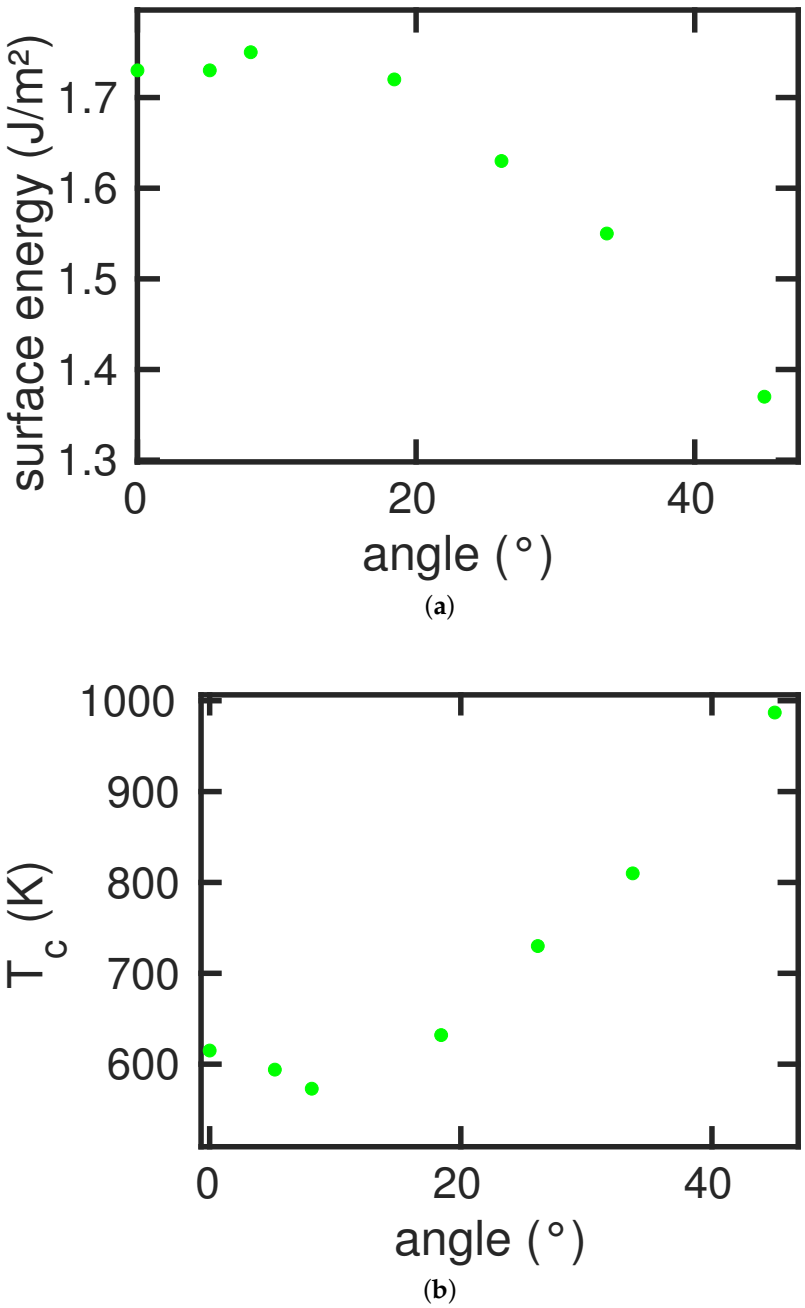

Figure 4. Dependence of the bcc specific surface energy (**a**); and the transition temperature of the austenitic phase transition T_c (**b**) on the tilt angle ϕ.

3.4.2. Transformation Path

A surface with a tilt angle of 0° transforms via the Bain path and a surface with a tilt angle of 45° with the Mao pathway. In this section, we present how intermediate surfaces transform.

Figure 5a,b answers this question for the example of the $(11\ 1\ 0)_{bcc}$ surface with a tilt angle of $\phi = 8.13°$. In this case the surface topography plays an important role. The surface features (100) facets, marked in Figure 5a, with defects (steps) in between. Four of these periodic defect structures fit into the size of the bcc specimen shown. After the transformation, the same number of four hcp plates were found in the transformed fcc sample; these can be seen as stacking fault planes in the dominant fcc structure. This demonstrates how the surface structure affects the transformation behavior.

For higher angles, the topography changed. The example of the $(3\ 2\ 0)_{bcc}$ surface with a surface angle of 33.69° is shown in Figure 5c,d. It is facetted featuring (110) facets. Now, the correlation between the six surface steps existing in the bcc structure of our simulation volume and the seven stacking fault lines generated in the transformed structure is less clear; the surface is no longer planar but shows a considerably roughened structure that is correlated with the stacking fault planes.

Figure 5e provides an overview of the fractions of hcp and fcc phase generated by the transformation. Beyond a tilt angle of 18°, hcp was the dominant phase generated. This is correlated with the fact that, beyond this angle, the Mao path is preferred, while, for smaller angles, where the fcc phase is favored, the systems follow the Bain pathway.

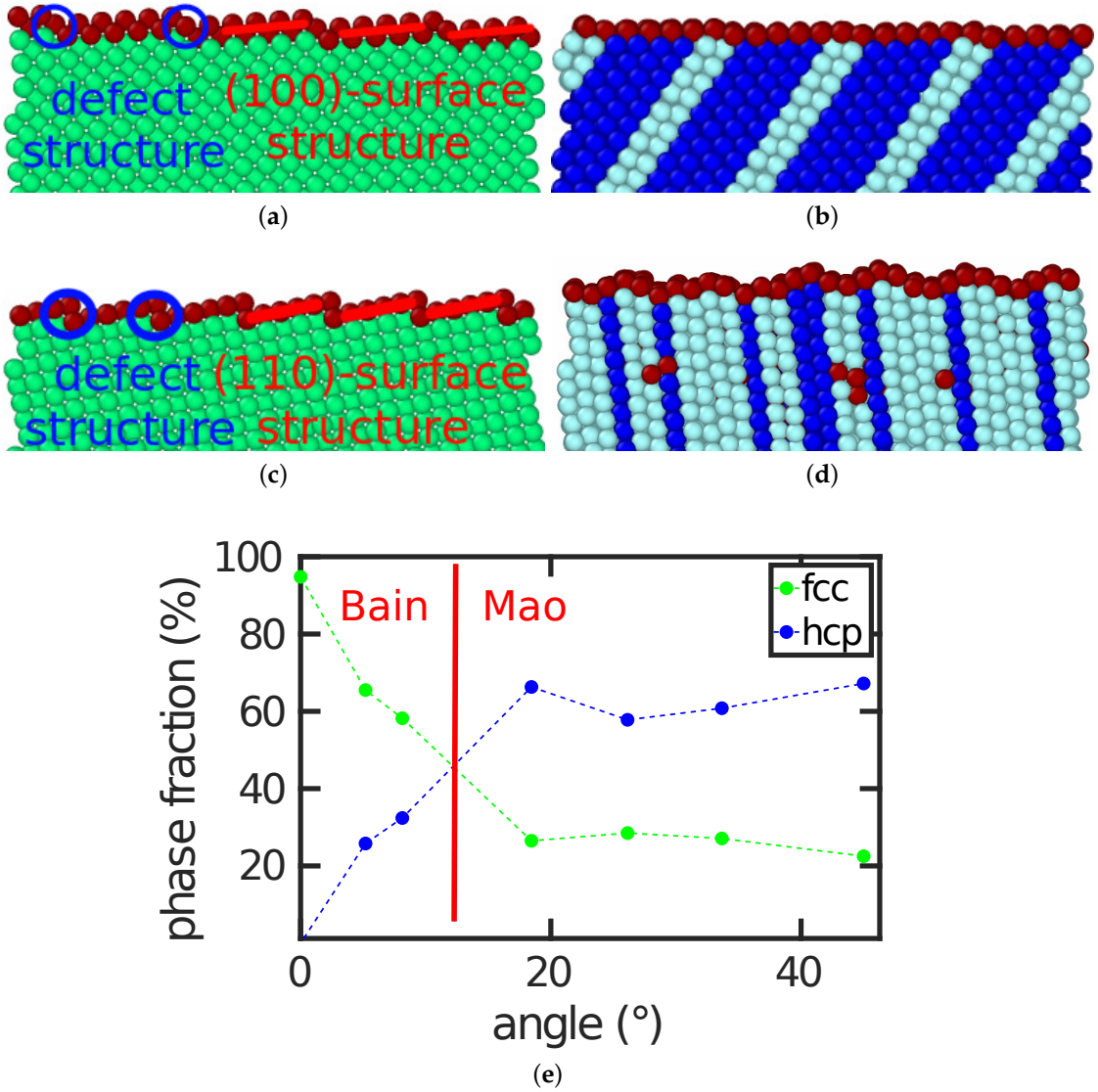

Figure 5. Side view of the thin film with a $(11\ 1\ 0)_{bcc}$ surface (**a**) before and (**b**) after the austenitic transformation; and (**c**,**d**) analogous for the $(3\ 2\ 0)_{bcc}$ surface. In the bcc structures (**a**,**c**), red lines highlight the dominant surface facets—$(100)_{bcc}$ and $(110)_{bcc}$, respectively—while blue circles show the steps. (**e**) The fraction of close-packed phases, fcc and hcp, after the transformation as a function of the tilt angle ϕ; the red line separates the regions where the Bain and the Mao path are followed. Colors denote the local lattice structure as in Figure 1.

In all the tilted surfaces investigated, the new phase nucleated at the surface. Figure 6 exemplifies this for the case of the $(7\ 1\ 0)_{bcc}$ surface, but we observed this nucleation path for all austenitic

transformations studied. This behavior appears plausible, since without a surface the bulk system would transform only at substantially higher temperatures, 1458 K.

As discussed above, high-energy surfaces have a tendency to nucleate the new phase earlier. This reduction can be explained firstly by the reduction in specific energy density (see Section 3.4.1) and secondly by the reduction in total surface area. The surface area of the transformed system decreased for all tilt angles; however, the reduction was reduced for larger ϕ, since more hcp phase was formed. While for $\phi = 0°$, the reduction of the surface area was 18 %, it was reduced to only 7 % for $\phi = 45°$.

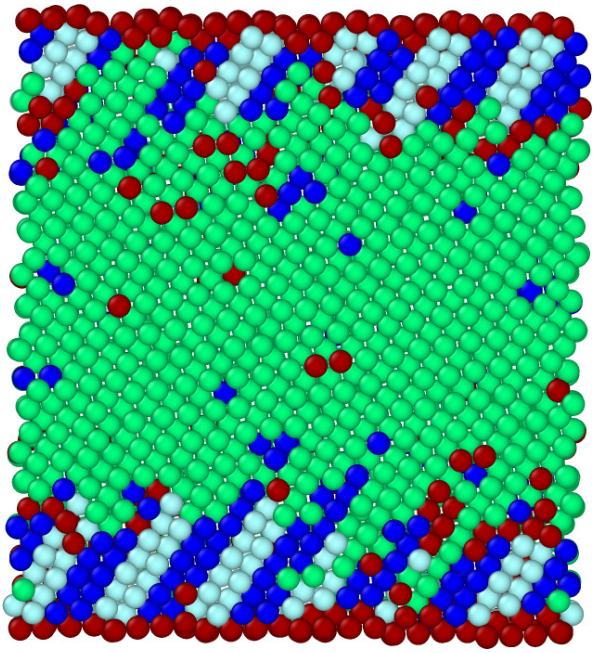

Figure 6. Side view of the thin film with a $(7\ 1\ 0)_{bcc}$ surface at the beginning of the austenitic transformation, highlighting the nucleation of the close-packed phases at the top surface. Colors denote the local lattice structure as in Figure 1.

4. Martensitic Transformation

In contrast to the austenitic transformation, in our simulations, the bulk fcc crystal under periodic boundary conditions did not transform martensitically under cooling. The reason hereto lies in the thermal fluctuations of the atom positions, which are necessary to overcome the kinetic barrier for nucleating the new phase. These were substantially smaller in the temperature range of the martensitic transformation than for the austenitic transformation. However, we show in this section that the presence of a surface can trigger the martensitic transformation. Note that, in an experiment, bulk fcc-Fe will transform as soon as the temperature falls below the equilibrium transition temperature, T_c, and a sufficient undercooling (of the order of 100 K) provides the necessary energy to surmount the strain energy arising from the volume difference of the two phases [41,42]. We emphasize that, in our present study, we investigated only the thermally induced transformation; the effect of mechanical load to induce the martensitic transformation has been studied elsewhere [12,34–36,43].

4.1. (100) Surface

Figure 7 shows the martensitic transformation of an fcc sample with a (100) surface. It transforms to a bcc crystal containing a microstructure. A detailed analysis (Figure 7c) shows that the structure is an ordered array of twins. The crystal deformation was small; the surface shrunk by 1 % by the phase transition. We note that the new phase nucleated at the surface.

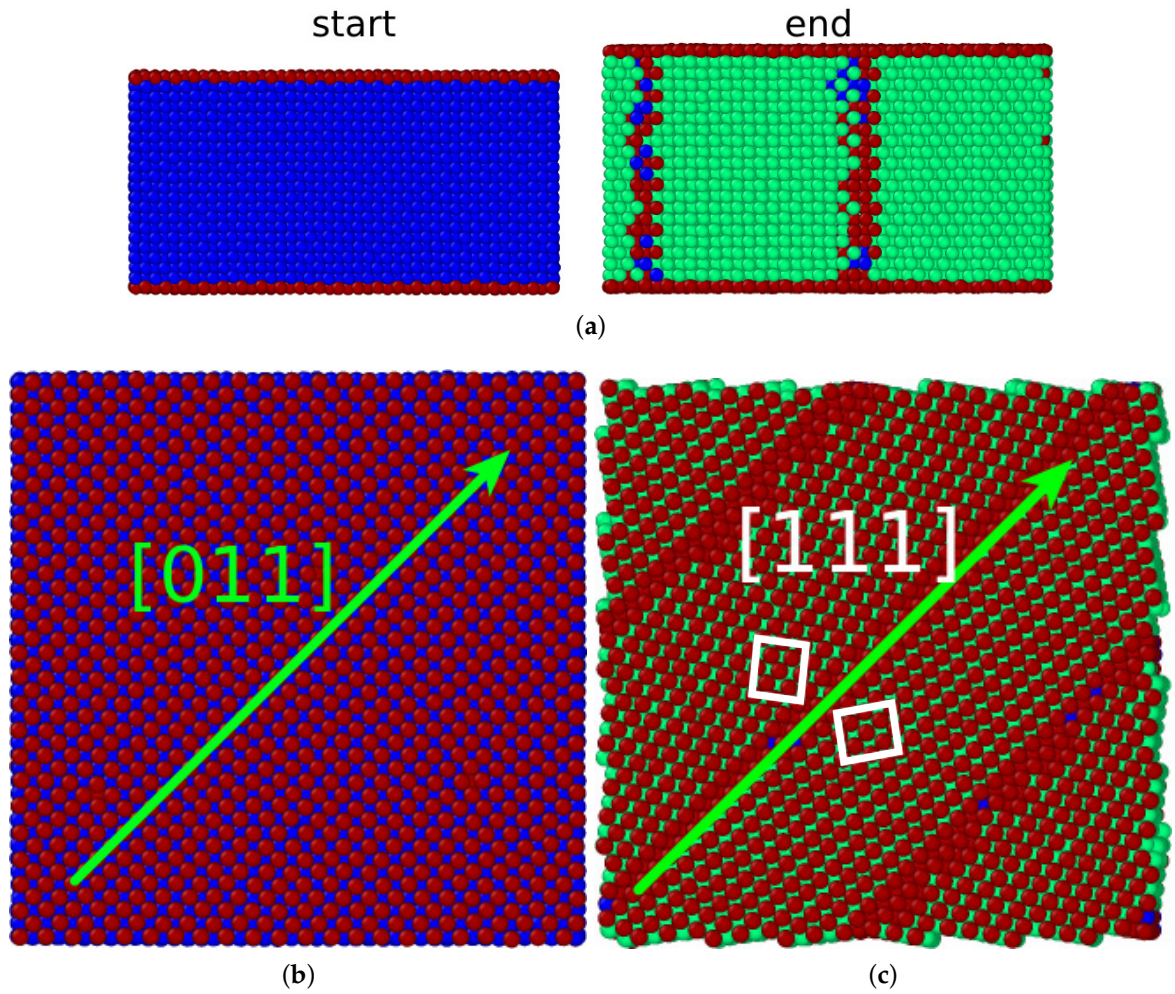

Figure 7. Martensitic transformation of a thin-film fcc Fe slab with a (100) surface: (**a**) side views of the film before and after the transformation; (**b**) top views of the film before the transformation; and (**c**) top views of the film after the transformation. The green arrows indicate the conserved directions, while the white rectangles highlight the twin structure. Colors denote local lattice structure as in Figure 1.

Figure 7b,c shows that the $(100)_{\mathrm{fcc}}$ surface was transformed into the close-packed $(01\bar{1})_{\mathrm{bcc}}$ plane. In addition, the close-packed directions were conserved: the $[011]_{\mathrm{fcc}}$ direction was transformed into the $[111]_{\mathrm{bcc}}$ direction. This is the signature of the Pitsch orientation relationship [44]:

$$(100)_{\mathrm{fcc}} \parallel (01\bar{1})_{\mathrm{bcc}}\,, \quad [011]_{\mathrm{fcc}} \parallel [111]_{\mathrm{bcc}}\,. \tag{6}$$

The twin boundaries established under the transformation are $(\bar{2}11)_{\mathrm{bcc}}$ planes.

In addition, in this transformation, the specific surface energy was reduced; here, the reduction was from a value of 1.57 J/m^2 for the $(100)_{\mathrm{fcc}}$ surface to a value of 1.35 J/m^2 for the $(110)_{\mathrm{bcc}}$ surface. This feature correlates well with the rather high martensitic transformation temperature of $T_c = 224$ K.

4.2. (110) Surface

Similar to the $(111)_{\mathrm{bcc}}$ surface, the $(110)_{\mathrm{fcc}}$ surface is not conserved under any orientation relationship. However, we observed a phase transition. In contrast to all other surfaces studied here, the flat surface structure was destroyed during the transition (cf. Figure 8a).

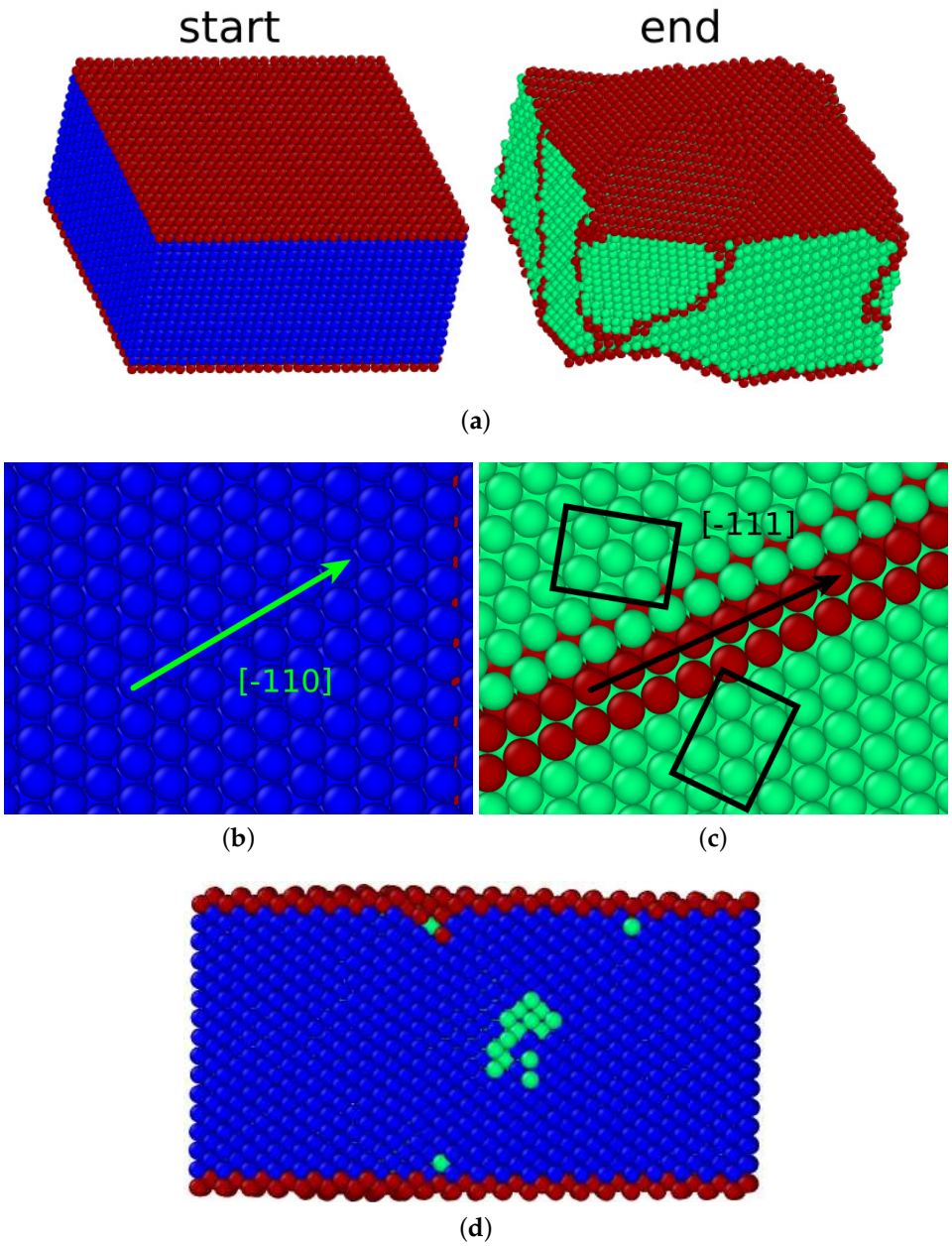

Figure 8. Martensitic transformation of a thin-film fcc Fe slab with a (110) surface: (**a**) perspective views of the film before and after the transformation; and (**b**,**c**) an oblique cut through the crystal where the close-packed $(111)_{\mathrm{fcc}}$ plane (**c**) transforms into the $(110)_{\mathrm{bcc}}$ plane (**d**). Here, the green (black) arrow highlights the conserved direction, while the black rectangles display the twin structure. (**d**) Side view of the film immediately after start of the transformation showing phase nucleation in the film interior. Colors denote the local lattice structure as in Figure 1.

In addition, this transformation conserved close-packed directions and planes. The $[\bar{1}10]_{\mathrm{fcc}}$ direction transformed into the $[\bar{1}11]_{\mathrm{bcc}}$ direction, as demonstrated in Figure 8b,c. This figure displays the close-packed $(111)_{\mathrm{fcc}}$ plane that transformed into the $(110)_{\mathrm{bcc}}$ plane. This is the signature of the Kurdjumov–Sachs orientation relationship [45]:

$$(111)_{\mathrm{fcc}} \parallel (110)_{\mathrm{bcc}}\,, \quad [\bar{1}10]_{\mathrm{fcc}} \parallel [\bar{1}11]_{\mathrm{bcc}}\,. \tag{7}$$

In the Kurdjumov–Sachs orientation relationship, usually twinning is observed. Indeed, Figure 8c shows the twin structure that developed under the transformation. The twin boundaries

were again built by $(112)_{bcc}$ planes. Under the Kurdjumov–Sachs orientation relationship, the surface plane cannot be conserved, resulting in the strongly distorted surface seen in Figure 8a after the transformation. The new surface is strongly facetted and consists of $\{100\}_{bcc}$ and $\{211\}_{bcc}$ planes. Consequently, the transformation did not start at the surface but in the bulk (see Figure 8d).

This transformation had a very low transformation temperature, 81 K. This is in line with the fact that the surface did not induce the transformation and did not even assist in nucleating the new phase, despite the relatively high surface energy of 1.73 J/m^2. However, note that, in a periodic volume, the martensitic transformation would not happen at all; hence, the presence of the surface, and its ability to provide free volume for coordinated atom movement, is key to facilitating the transformation.

4.3. (111) Surface

Similar to the case of the $(111)_{bcc}$ surface, the $(111)_{fcc}$ surface did not transform. This surface is close-packed with a small surface energy, 1.40 J/m^2. It was not conserved under any orientation relationship with the bcc phase.

4.4. Tilted Surfaces

Figure 9a shows the specific surface energy as a function of the tilt angle. Here, the $(100)_{fcc}$ surface has the lowest energy, 1.57 J/m^2, and the more open $(110)_{fcc}$ surface has a higher energy, 1.73 J/m^2. Due to surface facetting, tilted surfaces exhibit a maximum in surface energy, which occurs for tilt angles around 30°.

In this figure, we also show the dependence of the transformation path on the tilt angle. We observed the Pitsch path for angles below around 22.5° and the Kurdjumov–Sachs path at larger angles.

The dependence of the martensitic transformation temperature, T_c, on the tilt angle is displayed in Figure 9b. In contrast to the case of the austenitic transformation, here the transformation temperature did not follow the dependence of the surface energy. Rather, T_c decreased more or less continuously with the tilt angle. This shows that the surface energy was not the prime agent that influences the martensitic temperature. Here, the surface topography plays a decisive role. With increasing tilt angle, the surface included more $(110)_{fcc}$ facets; since $(110)_{fcc}$ surface was not conserved by the orientation relationships, nucleation of the new phase at the surface became harder and the transformation was delayed, decreasing the martensitic temperature. Thus, since the Kurdjumov–Sachs path, which operated here, does not conserve $(110)_{fcc}$ surface, the transformed surface became strongly facetted.

Note that a bulk system under periodic boundary conditions does not transform martensitically. This means that the presence of the surface also here induced the transformation; this is even true for the case of the $(110)_{fcc}$ surface, which was not conserved under the orientation relationships. We argue that it is the high surface energy of this surface that helped induce that transformation; as a counter-example, we mention the $(111)_{fcc}$ surface which has a low specific surface energy (1.40 J/m^2) and which does not feature any phase transformation.

We conclude that, in contrast to the austenitic transformation, where transition temperatures were dominated by the surface energy, the transformation path played a decisive role in the martensitic transformation. For dominating $(110)_{fcc}$ surface structure—that is for tilt angles beyond 22.5°—the Kurdjumov–Sachs path takes over and the transformation was increasingly delayed.

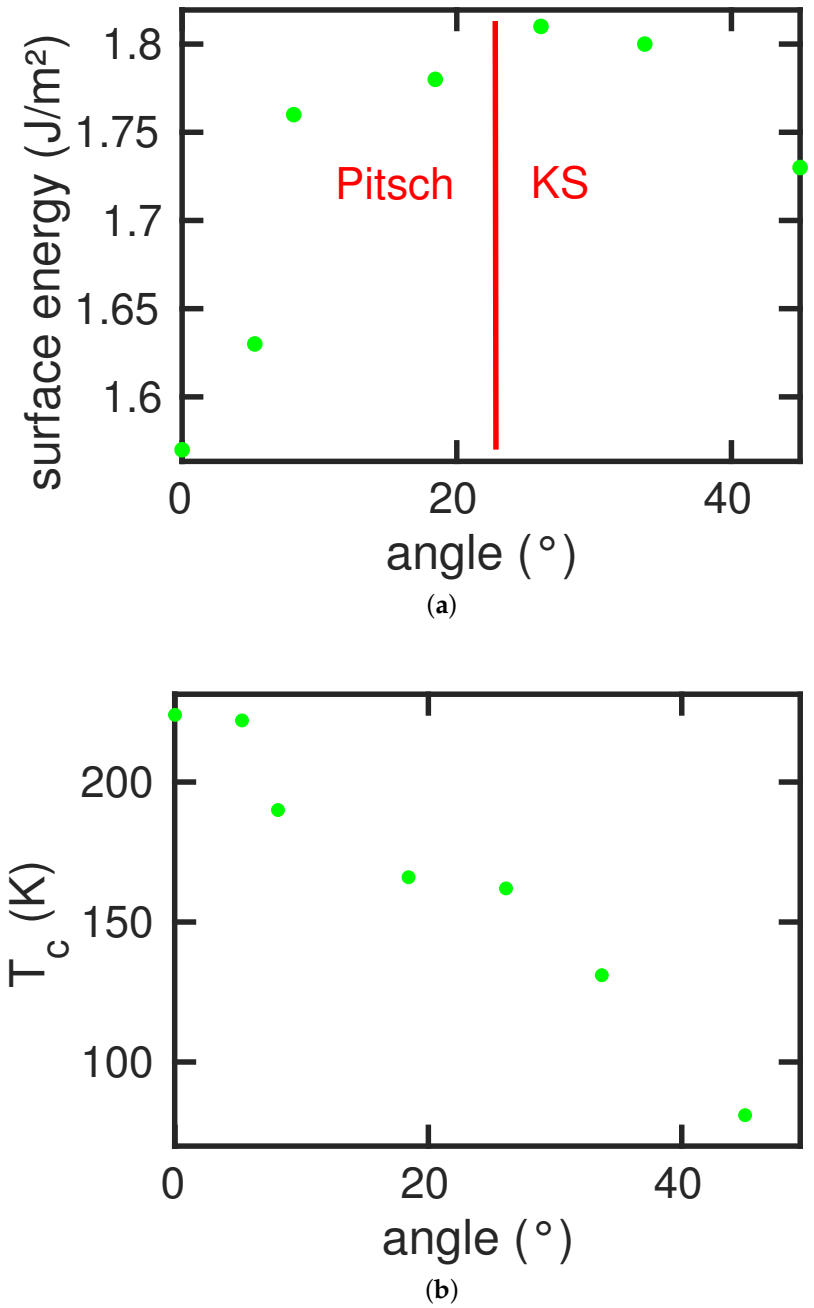

Figure 9. Dependence of the fcc specific surface energy (**a**) l and the transition temperature of the martensitic phase transition T_c (**b**) on the tilt angle ϕ. The red line in (**a**) separates the regions where the Pitsch and the Kurdjumov–Sachs (KS) paths are observed.

5. Conclusions

We studied the influence of free surfaces on the martensitic and austenitic phase transformation in iron. Using periodic boundary conditions, i.e., in the absence of free surfaces, the austenitic transformation occurs at 1458 K for the system size adopted in this study, while the martensitic transformation does not take place. For surfaces that are not conserved under any orientation relationship—such as $(111)_{\mathrm{bcc}}$ or $(111)_{\mathrm{fcc}}$—neither the martensitic nor the austenitic transformation occurs. This shows that orientation relations play an important role in starting the transition.

Indeed, for the single-indexed surfaces $(100)_{\mathrm{bcc}}$ and $(110)_{\mathrm{bcc}}$, the austenitic transformation starts easily. The transformation at these two surfaces follows simple transformation paths, namely the Bain

and the Mao et al. path, respectively. Higher-indexed surfaces, which interpolate between these two, show either of the transformation pathways, depending on the tilt angle.

Analogous behavior was observed for the martensitic transformation on the single-indexed surfaces $(100)_{\mathrm{fcc}}$ and $(110)_{\mathrm{fcc}}$. These transformations follow the Pitsch and the Kurdjumov–Sachs pathway, respectively. Again, tilted surfaces use the pathway of the neighboring single-indexed plane.

The austenitic transformation temperature follows well the specific surface energy of the native bcc phase. High-energy surfaces allow a quick nucleation of the close-packed phase, leading to a low transition temperature. Low-energy surfaces, which contain a high fraction of $(110)_{\mathrm{bcc}}$ facets, only transform at higher temperatures. In all cases, the new phase nucleates at the surface.

The martensitic transformation does not show this direct correlation with the surface energy. Here, the transformation temperature steadily decreases if the surface is tilted from the $(100)_{\mathrm{fcc}}$ to the $(110)_{\mathrm{fcc}}$ orientation. This is caused by the fact that the $(110)_{\mathrm{fcc}}$ surface is not a conserved plane under the Kurdjumov–Sachs pathway, which governs the transformation; consequently, the transformed surface shows a strong out-of-plane deformation. In this case, the new phase even nucleates in the bulk rather than close to the surface.

Author Contributions: J.M. performed the simulations and analyzed the results. J.M. and H.M.U. designed the work, discussed the results and wrote the manuscript.

Funding: This research was funded by the Deutsche Forschungsgemeinschaft via the Sonderforschungsbereich 926.

Acknowledgments: Access to the computational resources provided by the compute cluster"Elwetritsch" of the University of Kaiserslautern is appreciated.

Conflicts of Interest: The authors declare no conflict of interest.

Appendix A. Dependence on System Size

We studied the dependence of our simulation results on the size of the simulation volume for the representative case of the (710) surface.

Figure A1 displays the influence of the slab thickness d on the transformation temperature. A strong increase of the austenitic temperature and a decrease of the martensitic temperature with slab thickness was observed. Thus, both transformations are alleviated for thin slabs and impeded for thick slabs. Note that the slab thickness enters the average defect energy density quantified by

$$\epsilon_{\mathrm{defect}} = E_{\mathrm{surf}}/d. \tag{A1}$$

Hence, large defect energy densities lead to an earlier transformation, while small defect energies delay the transformation. We note that $d = 180$ Å was the thickest slab for which we could observe a martensitic transformation; at larger depths, the slab would not transform. For the austenitic transformation, we studied slab thicknesses up to 500 Å, and always observed a transformation, albeit at ever increasing temperature.

Additionally, we checked whether the transformation depends on the surface area of the simulation volume. Here, we used a slab of standard thickness, as described in Section 2, with a (710) surface. Increasing the surface area by extending the simulation crystallites in x direction (see Figure 1) up to 400% had no systematic influence on the austenitic or martensitic transformation temperatures; they only varied by <2 K around the average value of $T_c = 572$ (176) K for the austenitic (martensitic) temperature. This lack of influence is easy to rationalize: the periodic boundary conditions used in our simulations mimic an infinitely extended surface; different surface areas thus lead to the same transformation behavior. Finally, we note that the transformation pathway did not change when changing the slab thickness or the surface area of the simulation volume. The austenitic transformation always followed the Bain path, while the martensitic transformation followed the Pitsch path. In addition, in each case, the new phase nucleated at the surface.

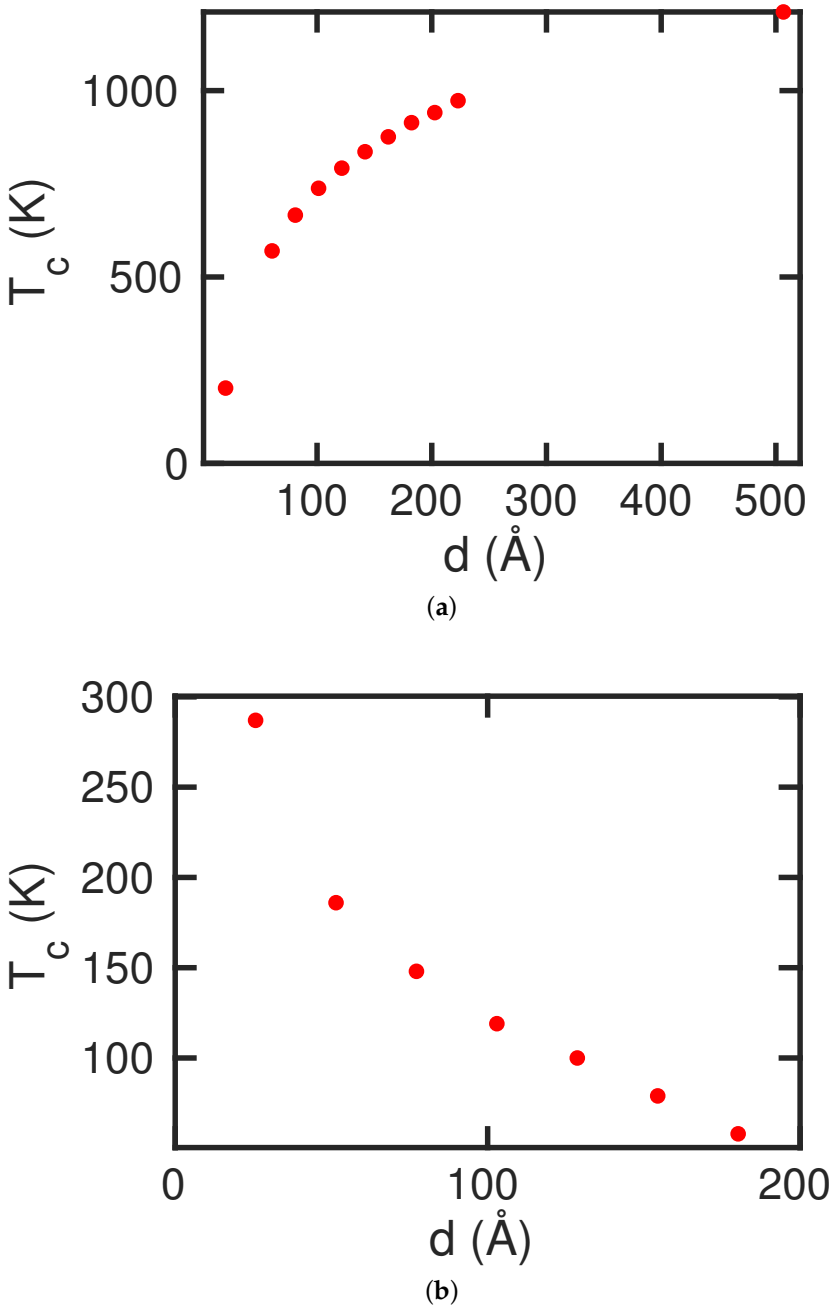

Figure A1. Dependence of the transformation temperature T_c on the thickness d of the slab: (**a**) austenitic transformation; and (**b**) martensitic transformation.

References

1. Pepperhoff, W.; Acet, M. *Constitution and Magnetism of Iron and its Alloys*; Springer: Berlin, Germany, 2001.
2. Pereloma, E.; Edmonds, D.V. (Eds.) *Phase Transformations in Steels*; Volume 2: Diffusionless Transformations, High Strength Steels, Modelling and Advanced Analytical Techniques; Woodhead Publishing Limited: Cambridge, UK, 2012.

3. Urbassek, H.M.; Sandoval, L. Molecular dynamics modeling of martensitic transformations in steels. In *Phase Transformations in Steels*; Pereloma, E., Edmonds, D.V., Eds.; Woodhead Publishing Limited: Cambridge, UK, 2012; Volume 2, pp. 433–463.
4. Ou, X. Molecular dynamics simulations of fcc-to-bcc transformation in pure iron: A review. *Mat. Sci. Technol.* **2017**, *33*, 822–835. [CrossRef]
5. Song, H.; Hoyt, J.J. A molecular dynamics study of heterogeneous nucleation at grain boundaries during solid-state phase transformations. *Comput. Mater. Sci.* **2016**, *117*, 151. [CrossRef]
6. Meiser, J.; Urbassek, H.M. Martensitic transformation of pure iron at a grain boundary: Atomistic evidence for a two-step Kurdjumov-Sachs-Pitsch pathway. *AIP Adv.* **2016**, *6*, 085017. [CrossRef]
7. Karewar, S.; Sietsma, J.; Santofimia, M.J. Effect of pre-existing defects in the parent fcc phase on atomistic mechanisms during the martensitic transformation in pure Fe: A molecular dynamics study. *Acta Mater.* **2018**, *142*, 71–81. [CrossRef]
8. Sharma, H.; Sietsma, J.; Offerman, S.E. Preferential Nucleation during Polymorphic Transformations. *Sci. Rep.* **2016**, *6*, 30860. [CrossRef]
9. Cahn, J.W. Nucleation on dislocations. *Acta Metall.* **1957**, *5*, 169–172. [CrossRef]
10. Dollins, C.C. Nucleation on dislocations. *Acta Metall.* **1970**, *18*, 1209–1215. [CrossRef]
11. Wang, B.; Urbassek, H.M. Phase transitions in an Fe system containing a bcc/fcc phase boundary: An atomistic study. *Phys. Rev. B* **2013**, *87*, 104108. [CrossRef]
12. Wang, B.; Urbassek, H.M. Molecular dynamics study of the α-γ phase transition in Fe induced by shear deformation. *Acta Mater.* **2013**, *61*, 5979–5987. [CrossRef]
13. Ou, X.; Sietsma, J.; Santofimia, M.J. Molecular dynamics simulations of the mechanisms controlling the propagation of bcc/fcc semi-coherent interfaces in iron. *Model. Simul. Mater. Sci. Eng.* **2016**, *24*, 055019. [CrossRef]
14. Maresca, F.; Curtin, W.A. The austenite/lath martensite interface in steels: Structure, athermal motion, and in-situ transformation strain revealed by simulation and theory. *Acta Mater.* **2017**, *134*, 302–323. [CrossRef]
15. Meiser, J.; Urbassek, H.M. Ferrite-to-Austenite and Austenite-to-Martensite Phase Transformations in the Vicinity of a Cementite Particle: A Molecular Dynamics Approach. *Metals* **2018**, *8*, 837. [CrossRef]
16. Wang, B.; Urbassek, H.M. Role of the Surface in Solid–Solid Phase Transitions: Molecular Dynamics Study of the α-γ Transition in Fe. *Metall. Mater. Trans. A* **2016**, *47*, 2471–2480. [CrossRef]
17. Levitas, V.I.; Javanbakht, M. Surface-Induced Phase Transformations: Multiple Scale and Mechanics Effects and Morphological Transitions. *Phys. Rev. Lett.* **2011**, *107*, 175701. [CrossRef] [PubMed]
18. Diao, J.; Gall, K.; Dunn, M.L. Surface-stress-induced phase transformation in metal nanowires. *Nat. Mater.* **2003**, *2*, 656. [CrossRef] [PubMed]
19. Hestenes, M.R.; Stiefel, E. Methods of Conjugate Gradients for Solving Linear Systems. *J. Res. Natl. Bur. Stand.* **1952**, *49*, 409. [CrossRef]
20. Nose, S. A unified formulation of the constant temperature molecular dynamics methods. *J. Chem. Phys.* **1984**, *81*, 511–519. [CrossRef]
21. Hoover, W.G. Canonical dynamics: Equilibrium phase-space distribution. *Phys. Rev. A* **1985**, *31*, 1695. [CrossRef]
22. Meyer, R.; Entel, P. Martensite-austenite transition and phonon dispersion curves of $Fe_{1-x}Ni_x$ studied by molecular-dynamics simulations. *Phys. Rev. B* **1998**, *57*, 5140. [CrossRef]
23. Engin, C.; Sandoval, L.; Urbassek, H.M. Characterization of Fe potentials with respect to the stability of the bcc and fcc phase. *Model. Simul. Mater. Sci. Eng.* **2008**, *16*, 035005. [CrossRef]
24. Sandoval, L.; Urbassek, H.M. Finite-size effects in Fe-nanowire solid-solid phase transitions: A molecular dynamics approach. *Nano Lett.* **2009**, *9*, 2290–2294. [CrossRef] [PubMed]
25. Sandoval, L.; Urbassek, H.M.; Entel, P. The Bain versus Nishiyama-Wassermann path in the martensitic transformation of Fe. *New J. Phys.* **2009**, *11*, 103027. [CrossRef]
26. Sandoval, L.; Urbassek, H.M.; Entel, P. Solid-solid phase transitions and phonon softening in an embedded-atom method model for iron. *Phys. Rev. B* **2009**, *80*, 214108. [CrossRef]
27. Plimpton, S. Fast Parallel Algorithms for Short-Range Molecular Dynamics. *J. Comput. Phys.* **1995**, *117*, 1–19. [CrossRef]
28. Honeycutt, J.D.; Andersen, H.C. Molecular dynamics study of melting and freezing of small Lennard-Jones clusters. *J. Phys. Chem.* **1987**, *91*, 4950–4963. [CrossRef]

29. Faken, D.; Jonsson, H. Systematic analysis of local atomic structure combined with 3D computer graphics. *Comput. Mater. Sci.* **1994**, *2*, 279–286. [CrossRef]
30. Stukowski, A. Visualization and analysis of atomistic simulation data with OVITO—The Open Visualization Tool. *Model. Simul. Mater. Sci. Eng.* **2010**, *18*, 015012. [CrossRef]
31. Grochola, G.; Russo, S.P.; Yarovsky, I.; Snook, I.K. "Exact' surface free energies of iron surfaces using a modified embedded atom method potential and lambda integration. *J. Chem. Phys.* **2004**, *120*, 3425. [CrossRef]
32. Schönecker, S.; Li, X.; Johansson, B.; Kwon, S.K.; Vitos, L. Thermal surface free energy and stress of iron. *Sci. Rep.* **2015**, *5*, 14860. [CrossRef]
33. Bain, E.C. The nature of martensite. *Trans. AIME* **1924**, *70*, 25.
34. Sandoval, L.; Urbassek, H.M. Solid-solid phase transitions in Fe nanowires induced by axial strain. *Nanotechnology* **2009**, *20*, 325704. [CrossRef] [PubMed]
35. Wang, B.; Urbassek, H.M. Computer simulation of strain-induced phase transformations in thin Fe films. *Model. Simul. Mater. Sci. Eng.* **2013**, *21*, 085007. [CrossRef]
36. Sak-Saracino, E.; Urbassek, H.M. Effect of uni- and biaxial strain on phase transformations in Fe thin films. *Int. J. Comp. Mat. Sci. Eng.* **2016**, *5*, 1650001. [CrossRef]
37. Mao, H.K.; Bassett, W.A.; Takahashi, T. Effect of pressure on crystal structure and lattice parameters of iron up to 300 kbar. *J. Appl. Phys.* **1967**, *38*, 272. [CrossRef]
38. Wang, F.M.; Ingalls, R. Iron bcc-hcp transition: Local structure from X-ray-absorption fine structure. *Phys. Rev. B* **1998**, *57*, 5647. [CrossRef]
39. Nishiyama, Z. Mechanism of transformation from face-centred to body-centred cubic lattice. *Sci. Rep. Tohoku Imp. Univ.* **1934**, *23*, 637.
40. Wassermann, G. Einfluß der α-γ-Umwandlung eines irreversiblen Nickelstahls auf Kristallorientierung und Zugfestigkeit. *Arch. Eisenhüttenwes* **1933**, *6*, 347. [CrossRef]
41. Kaufman, L.; Cohen, M. Thermodynamics and kinetics of martensitic transformations. *Prog. Metal Phys.* **1958**, *7*, 165–246. [CrossRef]
42. Fujita, F.E. Structural Phase Transformation. In *Physics of New Materials*, 2nd ed.; Fujita, F.E., Ed.; Springer: Berlin, Germany, 1998; Volume 27, Chapter 6, p. 141.
43. Sandoval, L.; Urbassek, H.M. Transformation pathways in the solid-solid phase transitions of iron nanowires. *Appl. Phys. Lett.* **2009**, *95*, 191909. [CrossRef]
44. Pitsch, W. The martensite transformation in thin foils of iron-nitrogen alloys. *Philos. Mag.* **1959**, *4*, 577–584. [CrossRef]
45. Kurdjumov, G.V.; Sachs, G. Über den Mechanismus der Stahlhärtung. *Z. Phys.* **1930**, *64*, 325–343. [CrossRef]